AIAA AVIATION Forum
June 27-July 1, 2022, Chicago, IL & Virtual
AIAA AVIATION 2022 Forum

10.2514/6.2022-3772

Design of High Width-Diameter Ratio Injection and Suction Ducts for Co-Flow Jet Airfoil

Paula A. Barrios * Yan Ren † GeCheng Zha ‡
Dept. of Mechanical and Aerospace Engineering
University of Miami, Coral Gables, Florida 33124
E-mail: gzha@miami.edu

May 3, 2022

Abstract

This paper conducts the design and analysis of injection and suction ducts for a 3D Co-Flow Jet (CFJ) airfoil with high ratio of slot width to micro-compressor diameter. A high ratio of the slot width to compressor diameter is desirable to reduce the number of the compressors along the wing span, but a high ratio also brings a challenge that the flow may separate near the side of the suction duct due to lower jet momentum in that region. The purpose of this paper is to design optimal ducts with maximized ratio of slot width to micro-compressor diameter and maximized total pressure recovery.

The performance of each duct design is simulated with a 3D CFJ airfoil at Mach number 0.25 for cruise condition at angle of attack 5°. In this study, a duct design of $W/D = 2.76$ displays a fully attached flow field and total pressure recoveries of 99% for injection duct and 99.1% for suction duct. Increasing to $W/D = 4.0$, the flow is still attached with the total pressure recoveries of 98.3% for the injection duct and 98.4% for the suction duct. At $W/D = 5.0$, there is a small flow separation at the corner of the airfoil before the flow goes into the suction duct. Some configuration variation is discussed to mitigate the flow separation.

Nomenclature

CFJ	Co-flow jet
AoA	Angle of attack
LE	Leading edge
TE	Trailing edge
S	Planform area
c	Airfoil chord
U	Flow velocity
q	Dynamic pressure $0.5\,\rho\,U^2$
p	Static pressure
$(\eta)_s$	Super ellipse shape parameter
a	Super ellipse semi major axis, duct width parameter
b	Super ellipse semi minor axis, duct height parameter
csa	duct cross-sectional area parameter
η	Pump efficiency

* Ph.D. Candidate
† PostDoc Researcher. Ph.D., AIAA member
‡ Professor, ASME Fellow, AIAA associate Fellow

ρ	Air density
$\dot{m}$	Mass flow rate
M	Mach number
ω	Pitching moment
P	Pumping power
SD	Suction duct
ID	Injection duct
∞	Free stream conditions
j	Jet conditions
C_L	Lift coefficient $L/(q_\infty S)$
C_D	Drag coefficient $D/(q_\infty S)$
C_M	Moment coefficient
C_μ	Jet momentum coefficient $\dot{m}_j U_j /(q_\infty S)$
$(C_L/C_D)_c$	CFJ airfoil corrected aerodynamic efficiency $L/(D + P/V_\infty)$
$(C_L^2/C_D)_c$	CFJ airfoil productivity efficiency $C_L^2/(C_D + P/V_\infty)$
P_C	Power coefficient $L/(q_\infty S V_\infty)$
P_{tr}	Total pressure ratio between injection and suction
M_∞	Free stream Mach number
M_{isen}	Isentropic Mach number
P_{tinj}	Total injection pressure
P_{tsuc}	Total suction pressure
V_{inj}/V_∞	Normalized injection velocity

1 Introduction

Minimizing energy consumption of airlines centers on high cruise efficiency. Active flow control (AFC) is a promising method to enhance aerodynamic performance. Enhancing cruise efficiency requires AFC to have low energy expenditure with high conversion efficiency. Most efforts to improve cruise efficiency have been made by passive flow controls, including winglet, wing body combination, flying wing configurations, boundary layer ingestion, distributed propulsion, etc. Not much progress has been made to improve subsonic airfoil cruise performance efficiency through AFC.

AFC transfers external energy to the controlled flow to improve the performance of the flow system. For all AFC systems, there are three measures of merit (MoM): 1) effectiveness, 2) power required (PR), and 3) power conversion efficiency (PCE). Effectiveness quantifies performance enhancement, e.g., removal of flow separation, drag reduction, lift increase, stall prevention, noise mitigation, etc. Power required quantifies the AFC power needed to achieve the targeted effectiveness. Power conversion efficiency quantifies the efficiency to convert the external energy (e.g., mechanical, electric, chemical) to energy required by the controlled flow. It determines how much total power will be consumed by the actual flow control system. For AFC to benefit industry realistic applications, all three MoM matter. The ultimate criterion for an AFC is that the system efficiency gain should be greater than the AFC energy expenditure.

The Co-Flow Jet (CFJ) airfoil, shown in figure 1 is a zero-net mass-flux (ZNMF) AFC method developed by Zha et al. [1, 2, 3, 4, 5, 6, 7, 8, 9, 10, 11] that can dramatically increase lift coefficient, stall angle of attack, and drag reduction. For the CFJ AFC, a small amount of mass flow is withdrawn into the suction duct located near the TE, pressurized and energized by the micro-compressor, and injected near the LE tangentially to the main flow through the injection slot.

The flow of CFJ active flow control airfoil is delivered by micro-compressor actuators via injection and suction

ducts as shown in figure 1, which have the cross section shape transitioning from a circle, matching the micro-compressor diameter, to a rectangle slot to inject and withdraw the flow. The duct design with a high ratio of the slot width to compressor diameter W/D (see figure 1) is desirable to reduce the number of compressors along the wing span. But, a high ratio also brings a challenge that the flow may be separated near the side of the suction duct due to lower jet momentum in that region. The micro-compressor causes a swirl effect on the flow as it exits. The injection duct requires a duck-bill shaped centerbody to guide the flow and remove any flow separation. As the ratio becomes higher, it is important to push the flow more towards the sides of the injection duct [12]. The suction duct also requires a centerbody, shaped as a bullet, to lead the flow into the micro-compressor. Design requirements include no flow separation and as high as possible total pressure recovery.

The low energy expenditure required by the CFJ enables it to improve cruise productivity efficiency, $C_L^2/(C_D + P_C)$, substantially compared with conventional design (P_C is the required power coefficient). In other words, CFJ is proven to have high effectiveness and low power required. The actual power consumed by the micro-compressor is $P_{act} = P_C/\eta$, where η is the compressor power conversion efficiency. This paper addresses the second MoM, which requires minimizing the power required P_C of the CFJ airfoil system. P_C is determined by the CFJ airfoil and by the ducts. The CFJ airfoil adopted is previously designed by Wang et al. [13, 14, 15]. The focus of this paper is to optimize the ducts design.

The flow within the ducts is essential to achieve high CFJ aerodynamic performance. Any flow separation will increase the energy expenditure of the system. Although this paper focuses on duct design, the whole 3D CFJ airfoil with ducts is simulated to have the integrated effect of the airfoil and the ducts system to include the interaction effect. Simulating the ducts only does not realistically describe the interaction of the ducts with the airfoil. The purpose of this paper is two-fold: 1) to design optimal ducts with maximized ratio of slot width to micro-compressor diameter, W/D; 2) maximize total pressure recovery to achieve optimal conversion efficiency.

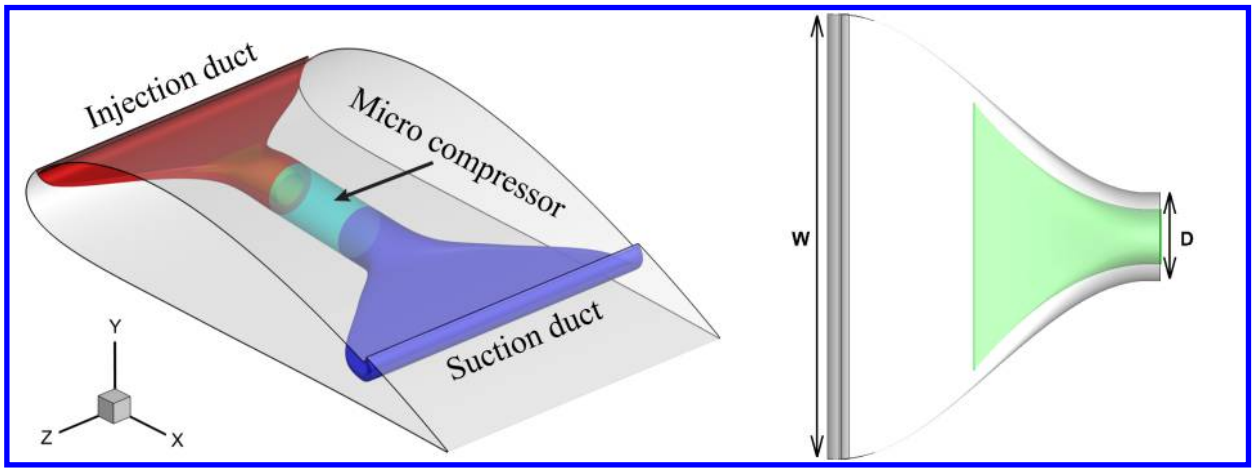

Figure 1: Schematic of CFJ setup within the airfoil

2 Methodology

2.1 Lift and Drag Calculation

In a CFD analysis, the total aerodynamic forces and moments are determined by the force surface integral and jet reactionary force. The reactionary force of a CFJ airfoil is calculated through flow parameters obtained from the injection and suction slots. The equations for lift and drag due to the jet reactionary force are given by Zha et al. [2] using the control volume analysis in figure 2:

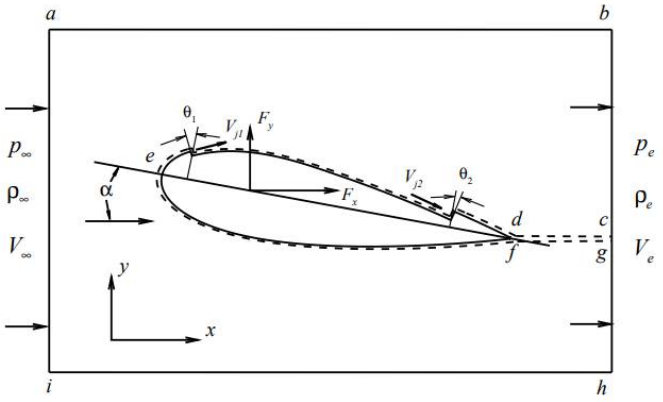

Figure 2: Control volume of a CFJ airfoil

$$F_{x_{cfj}} = (\dot{m}_j V_{j1} + p_{j1} A_{j1}) * cos(\theta_1 - \alpha) - (\dot{m}_j V_{j2} + p_{j2} A_{j2}) * cos(\theta_2 + \alpha) \tag{1}$$

$$F_{y_{cfj}} = (\dot{m}_{j1} V_{j1} + p_{j1} A_{j1}) * sin(\theta_1 - \alpha) + (\dot{m}_{j2} V_{j2} + p_{j2} A_{j2}) * sin(\theta_2 + \alpha) \tag{2}$$

where the subscript 1 indicates the injection slot and subscript 2 denotes the suction slot, θ_1 and θ_2 are the angles between the slot's surface and a line normal to the chord, and α is the angle of attack.

Total lift and drag are given by the following equations:

$$D = R'_x - F_{x_{cfj}} \tag{3}$$

$$L = R'_y - F_{y_{cfj}} \tag{4}$$

where R'_x and R'_y are surface integrals of pressure and shear stress in the x_{drag} and y_{lift} directions. For a 3D CFJ wing, total lift and drag are determined by integrating the drag and lift equations in the spanwise direction.

2.2 Jet Momentum Coefficient

C_μ, or the jet momentum coefficient, quantifies the jet intensity and is defined by,

$$C_\mu = \frac{\dot{m} V_j}{\frac{1}{2} \rho_\infty {V_\infty}^2 S} \tag{5}$$

where $\dot{m}$ is the injection mass flow rate, V_j is the mass-averaged injection velocity, ρ_∞ is the free stream density, V_∞ is the free stream velocity, and S is the planform area.

2.3 Power Coefficient

In a CFJ airfoil, a system of micro-compressors are embedded inside of the wing. The compressors take air from the suction slot and and eject the air through the injection slot. The power consumption is determined by the jet mass flow and total enthalpy change through:

$$P_{CFJ} = \dot{m}(H_{t1} - H_{t2}) \tag{6}$$

where H_{t1} and H_{t2} are the mass-averaged total enthalpy in the injection and suction slots, P is the power required by the micro-compressor, and $\dot{m}$ the jet mass flow rate. The power consumption of Eq. (6) can be also expressed by the following equation,

$$P_{CFJ} = \frac{\dot{m} C_p T_{t2}}{\eta} (\Gamma^{\frac{\gamma-1}{\gamma}} - 1) \tag{7}$$

where γ is the specific heat ratio, or 1.4 for ideal gas, and η is the isentropic pumping efficiency. Γ is the total pressure ratio of the pump defined as $\Gamma = \frac{P_{t1}}{P_{t2}}$, where P_{t1} and P_{t2} are the mass-averaged total pressures in the injection and suction slots, respectively. The power coefficient for a CFJ airfoil is then,

$$P_{C,CFJ} = \frac{P_{CFJ}}{\frac{1}{2}\rho_\infty V_\infty^3 S} \tag{8}$$

The power coefficient for a propeller actuator is given by,

$$P_P = \frac{2}{\rho V_\infty^3 S} \sqrt{\frac{F^3}{2\rho A}} \tag{9}$$

where F is the total force generated by the propeller actuator perpendicular to the propeller disk, and A is the area of the actuator disk. The propeller power coefficient can also be given by the absolute value of the drag coefficient because the propeller thrust should overcome the drag at cruise.

The power coefficient due to CFJ and the propeller actuator can be combined as,

$$P_C = P_{C,CFJ} + P_P \tag{10}$$

but since no propeller is being utilized in this study, $P_P = 0$ and the power coefficient is only due to the CFJ airfoil.

2.4 Corrected Aerodynamic Efficiency

For a conventional airfoil, the wing aerodynamic efficiency is defined as:

$$\frac{L}{D} \tag{11}$$

and for a CFJ wing, the pure aerodynamic relationship between lift and drag still follows Eq. (11). However, since CFJ AFC expends energy, the above is modified to consider the energy consumption of the micro-compressor. The corrected aerodynamic efficiency is:

$$\frac{C_L}{C_{Dc}} = \frac{C_L}{C_D + P_C} \tag{12}$$

where C_{Dc} is the equivalent drag coefficient that includes the drag of the aircraft system and the power required by the CFJ.

2.5 Aircraft Productivity

The productivity efficiency C_L^2/C_D is used to measure the productivity of an airplane characterized by the product of an aircraft's range and its weight [16]. It is a more thorough parameter than C_L/C_D in determining the merit of aerodynamic design during cruise. Aircraft productivity includes the ratio of lift to drag coefficient and the aircraft weight from C_L. The corrected productivity efficiency for CFJ airfoils is defined as,

$$\frac{C_L^2}{C_{Dc}} = \frac{C_L^2}{C_D + P_C} \tag{13}$$

2.6 Airfoil Geometry

The airfoil is developed based on the NACA 6421 airfoil. The CFJ injection and suction slot sizes are normalized by the airfoil chord length (C). The original airfoil design, CFJ6421-SST150-SUC247-INJ117, created by Wang et. al. [13, 14, 15] was used as a starting point. It has an injection slot size of 1.17%C and suction slot size of 2.47%C. However, during design iterations, the suction slot height was decreased by 30% to reduce flow separation occurring within the duct. The current airfoil used in this study is CFJ6421-SST150-SUC173-INJ117.

2.7 Duct Geometry

The CFJ airfoil injection and suction slot locations are determined according to previously published 2D designs [13, 14, 15]. The injection and suction duct meanlines are determined based on the slot locations. The ducts have a circular shape at the compressor interface and then become rectangular at the slots. The method of calculating circular-to-rectangular transition surfaces developed in [17] and used by [18, 19] is adopted. Superellipses are created along the duct meanlines, shown in figure 3. The duct surfaces are formed by connecting those cross sections. Circles, ellipses, and rectangles are cases of superellipses, made up by the locus of points defined by,

$$(\frac{y}{a})^{(\eta)_s} + (\frac{z}{b})^{(\eta)_s} = 1 \tag{14}$$

where a is the semi major axis, b is the semi minor axis, and $(\eta)_s$ is the shape parameter. The rectangle shape is represented by $(\eta)_s = 100$ and a circle is $(\eta)_s = 0$. Parameters a and b are also the half width and half height of the duct cross section respectively. These are continuous analytic functions of x, the axis distance from the duct inlets. Transition surfaces are found by iteratively computing $(\eta)_s(x)$ from equation 14.

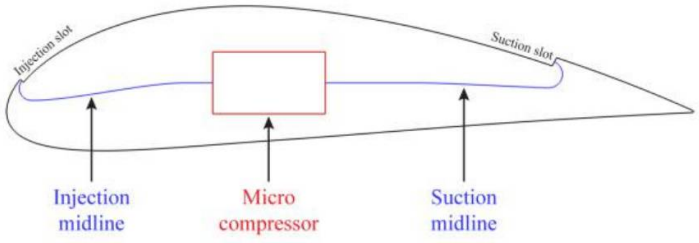

Figure 3: General schematic of CFJ airfoil configuration

The mathematical model allows the configuration of the duct geometry and identifies the parameters for duct design. Converging ducts have a favorable pressure gradient and are easier to design than diverging ducts, which are prone to flow separation. When designing the injection duct, the duck-bill centerbody design is important since it is used to guide the swirl flow exiting the micro-compressor and prevents flow separation. The width design of the injection duct is also crucial to remove separation prior to the suction duct. Key parameters in suction duct design are the area and width of the duct. Suction also has a bullet centerbody that will guide the flow into the micro-compressor. Another principle parameter is the slot width to compressor diameter ratio W/D which is a major influence to duct performance.

2.8 Total Pressure Recovery

Duct design is an integral part of the consolidation of the system, requiring a high as possible total pressure recovery and healthy air flow throughout. Total pressure recovery is defined as,

$$P_{tr} = \frac{\oiint_{S_o} \rho V P_{02} dA}{\oiint_{S_i} \rho V P_{01} dA} \tag{15}$$

where S_o and S_i are the cross section interface at outlet and inlet respectively. P_{02} and P_{01} are the total pressure evaluated at outlet and inlet. A high total pressure recovery signifies minimal loss within the duct. For injection ducts, the total pressure decreases toward the injection slot while for suction ducts the total pressure decreases toward the compressor interface. In general, the total pressure recovery of injection ducts is smaller than suction ducts due to the swirl flow and the centerbody increasing the energy loss [18].

2.9 CFD Simulation Setup

The FASIP (Flow-Acoustics-Structure Interaction Package) CFD code is used for the numerical simulation. The 3D Reynolds Averaged Navier-Stokes (RANS) equations with one-equation Spalart-Allmaras [20] turbulence model is used. A 3rd order WENO scheme for the inviscid flux [21, 22, 23, 24, 25, 26] and 2nd order central differencing for the viscous terms [21, 25] are utilized to discretize the Navier-Stokes equations. The low diffusion E-CUSP scheme used as the approximate Riemann solver suggested by Zha et al. [22] is utilized with the WENO scheme to evaluate the inviscid fluxes. Implicit time marching method using Gauss-Seidel line relaxation is used to achieve a fast convergence rate [27]. Parallel computing is implemented to save wall clock simulation time [28].

2.10 Boundary Conditions

The 3rd order accuracy no slip condition is enforced on the solid surface with the wall treatment suggested in [29] to achieve flux conservation on the wall. Symmetric boundary conditions are utilized on the two boundaries in the span direction. Total pressure, total temperature and flow angles are specified at the injection duct inlet based on the profile of the micro-compressor at the outlet. The total pressure, total temperature, and flow angle are also specified at the upstream portion of the far field based on free stream condition. Constant static pressure is applied at the suction duct outlet as well as the downstream portion of the far field. Cross section faces of the ducts are meshed with an "H" topology, 300 points in the streamwise direction, 60 points radially, and 90 points in the circumferential direction. Each duct has a mesh size of 1.62 million points, split into 20 blocks. The total mesh size, shown in figure 4 for the CFJ airfoil at Mach number 0.25 is 5.68 million points, split into 135 blocks for the parallel computation. The first grid point on the wing surface is placed at $y^+ \approx 1$.

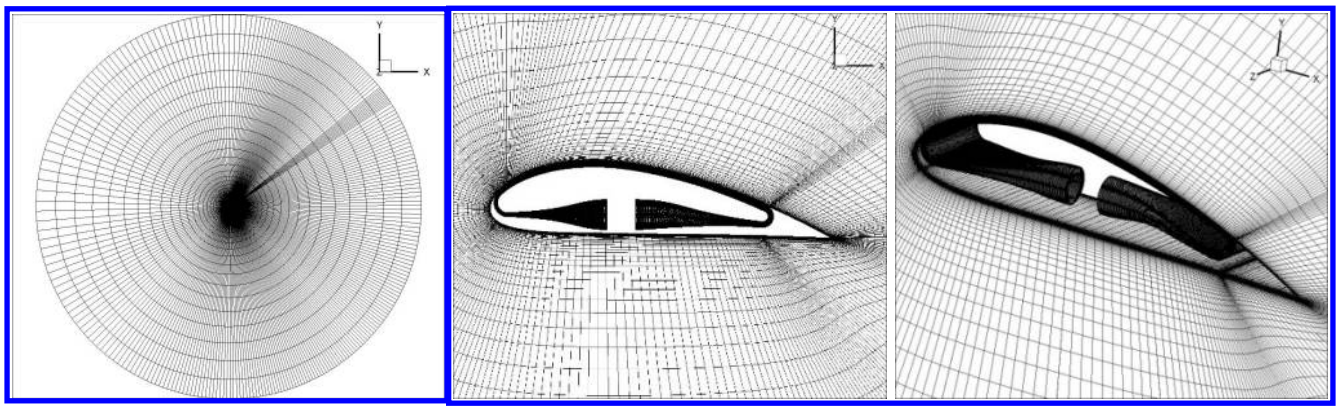

Figure 4: Mesh topology of 3D CFJ airfoil with injection and suction ducts

3 Results and Discussion

3.1 Steps for the Integrated Design

The integrated design steps are as follows:

1. CFJ wing design: 2D CFJ airfoil and 3D CFJ wing are designed to meet the aircraft mission requirements for takeoff, cruise, and landing with optimal performance. The design provides the requirements of wing dimensions, micro-compressor mass flow rate, and total pressure ratio.

2. Micro-compressor design: A micro-compressor is then designed to satisfy the required total pressure ratio and the dimensions of the airfoil with maximized mass flow rate, highest efficiency, and largest operating range from choke limit to stall limit.

3. Duct design: The CFJ injection and suction ducts are then designed to match the airfoil dimensions with the boundary conditions from the micro-compressor and the CFJ wing flow conditions, no flow separation inside the ducts, and minimum total pressure loss.

4. Integrate the ducts with the 3D CFJ airfoil using the micro-compressor flow conditions at the CFJ injection inlet (micro-compressor outlet) and suction outlet (micro-compressor inlet). Simulate the 3D CFJ airfoil with the ducts designed in Step 3.

5. Examine the results and the aerodynamic performance. If satisfied, stop; if not satisfied, return to Step 1 and repeat the process.

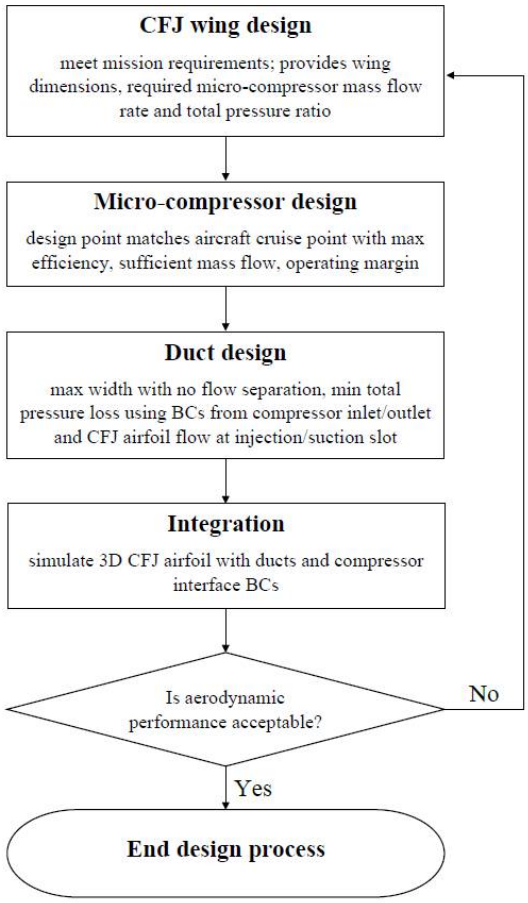

Figure 5: Flowchart of the integrated design process

This paper conducts Steps 3, 4, and 5.

3.2 CFJ Injection and Suction Ducts

In order to integrate a micro-compressor with the CFJ airfoil, the injection and suction ducts must be designed according to the following:

1. Match the mass flow requirement for the required C_μ.
2. No flow separation inside the ducts to minimize total pressure loss and maximize flow uniformity at the injection slot.
3. Maximize slot width to minimize the number of micro-compressors to be used. However, a large ratio of slot width to compressor diameter, W/D, will also make the flow prone to separation.

Three different designs are studied in this paper: (a)$W/D = 2.76$, (b)$W/D = 4.0$, and (c)$W/D = 5.0$. Figure 6 describes the width parameter a, height parameter b, and cross-sectional area csa, distributions for the injection and suction designs based on Eq. (14). The csa denotes the difference between the area of the duct and the centerbody. Table 1 shows the ratio of the duct inlet to outlet. For the injection duct, it means the ratio of the compressor outlet area to the injection slot area on the airfoil. For the suctions duct, it is the opposite. The ratio means the ratio of the suction slot area to the compressor inlet area. Note the compressor inlet and outlet area

do not have to be the same. In this paper, they are treated to be the same. Table 1 indicates that both ducts are converging for $W/D = 2.76$ while for the higher W/D ratios, injection duct diverges and suction duct converges. The height parameter b distribution is the same for all the designs.

The design of $W/D = 2.76$ is adopted from [30, 31] and is used as a reference for the higher ratio designs since it has proven to have a healthy attached flow field. The designs for $W/D = 4.0$ and 5.0 went through a number of different iterations to improve performance. The injection designs try to mimic a similar width a distribution as $W/D = 2.76$ and use the same centerbody design. All three suction ducts have the same centerbody design. The higher width to diameter designs show a sharp slope of the width a at the suction inlet, as opposed to $W/D = 2.76$, in order to have a faster converging area *csa* in an attempt to improve the flow field entering the suction duct.

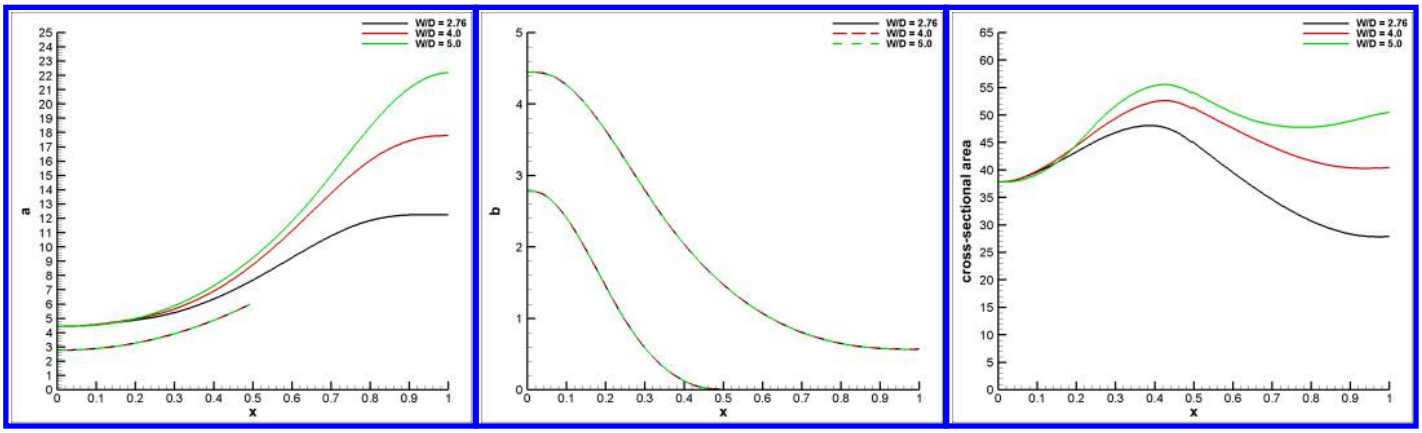

(a)

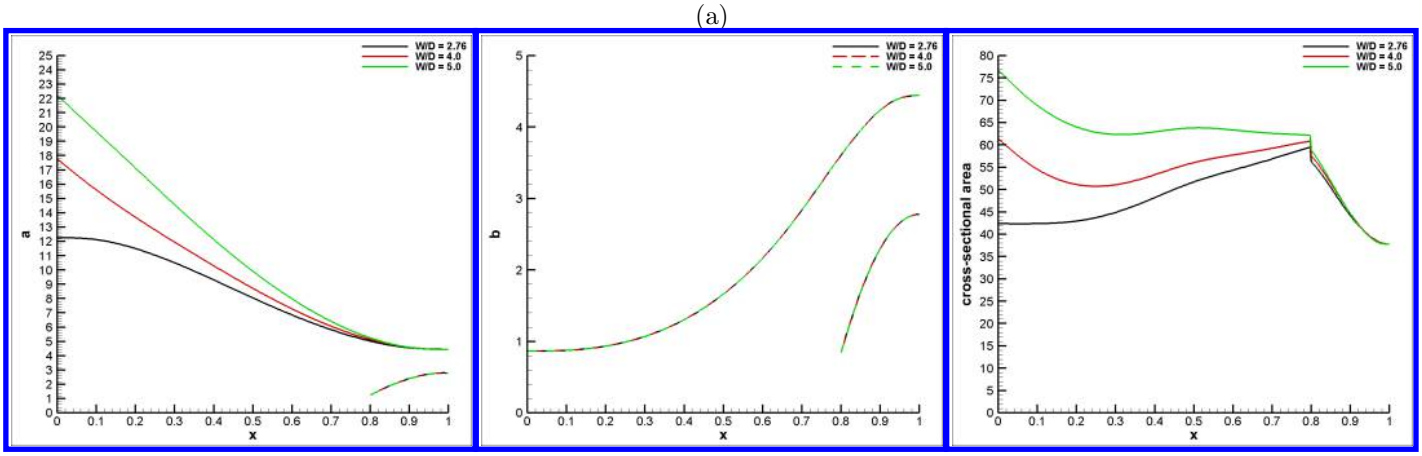

(b)

Figure 6: Profiles of width, height, and cross sectional area for (a)injection and (b)suction for W/D =2.76, 4.0, and 5.0

Table 1: Area ratios of the injection and suction ducts from inlet to outlet

W/D	*Injection*	*Suction*
2.76	1.36	1.12
4.0	0.94	1.62
5.0	0.75	2.03

Figure 7 shows the geometries of the three designs. The centerbody of the injection duct has a duck-bill shape,

to guide the swirl flow from the micro-compressor to prevent flow separation as per [18, 19]. A bullet-shaped centerbody is added to the suction duct to make the flow enter the micro-compressor.

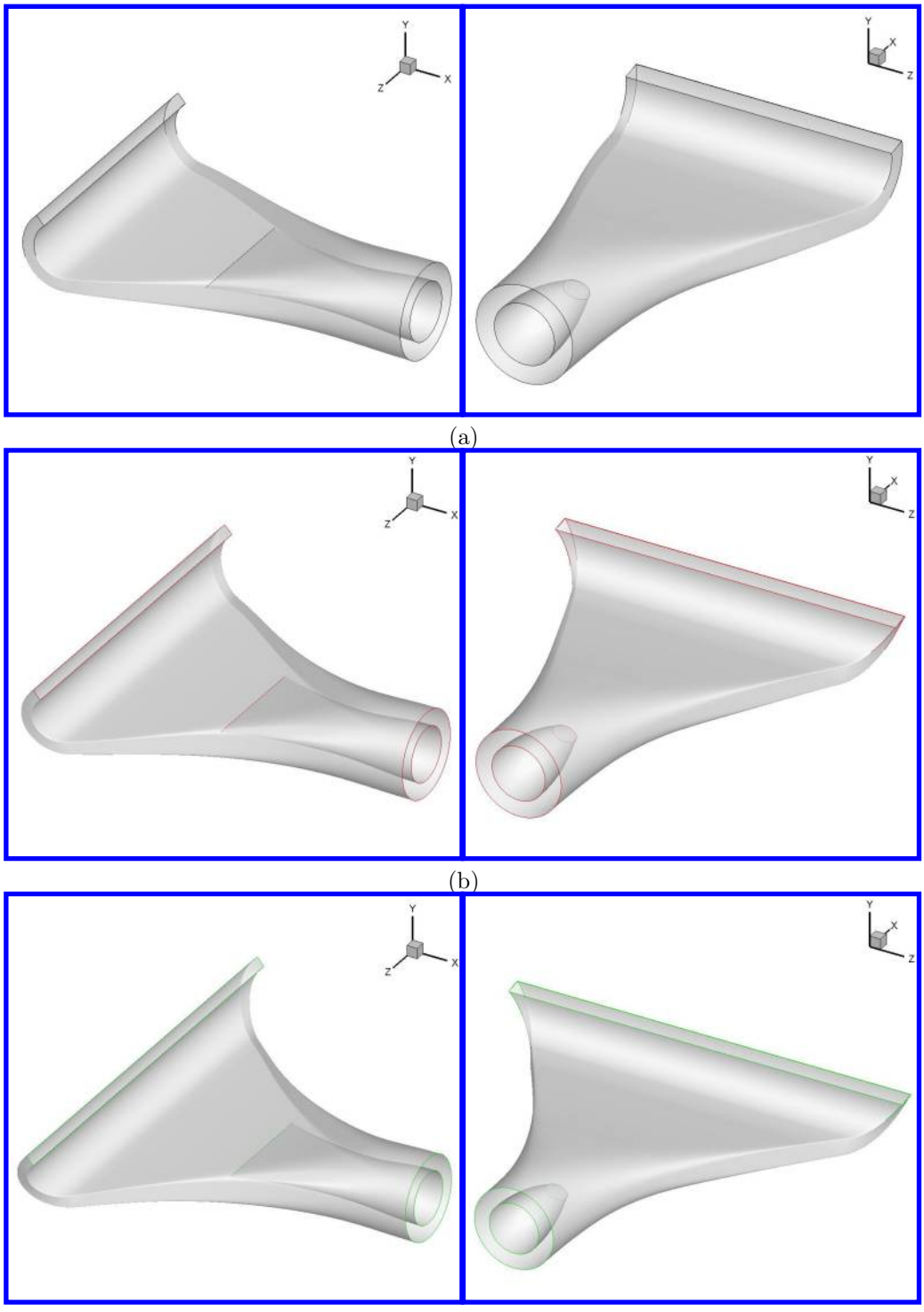

Figure 7: Geometry of injection (left) and suction (right) ducts for design (a)$W/D = 2.76$, (b)$W/D = 4.0$, and (c)$W/D = 5.0$

The ducts are integrated into the CFJ airfoil and simulated at $M = 0.25$ and $AoA = 5^{\circ}$ and C_{μ} of 0.03. Figure 8 shows Mach contours at the mid-span of the airfoil system. Here, the centerbody shape for both ducts is clear. From these figures, $W/D = 2.76$ displays a low Mach number region as the flow approaches over the suction centerbody. Designs (b) and (c) show the flow getting progressively stronger within the ducts as the width increases. Figure 9 shows the Mach number contours for the duct and suction surfaces of each design. It is clear that with larger W/D, separation and weak flow occur on the suction surface at the corners just before the suction duct inlet. So, with increasing width, the flow in the middle of the airfoil becomes stronger but becomes weaker near the two sides of the slots.

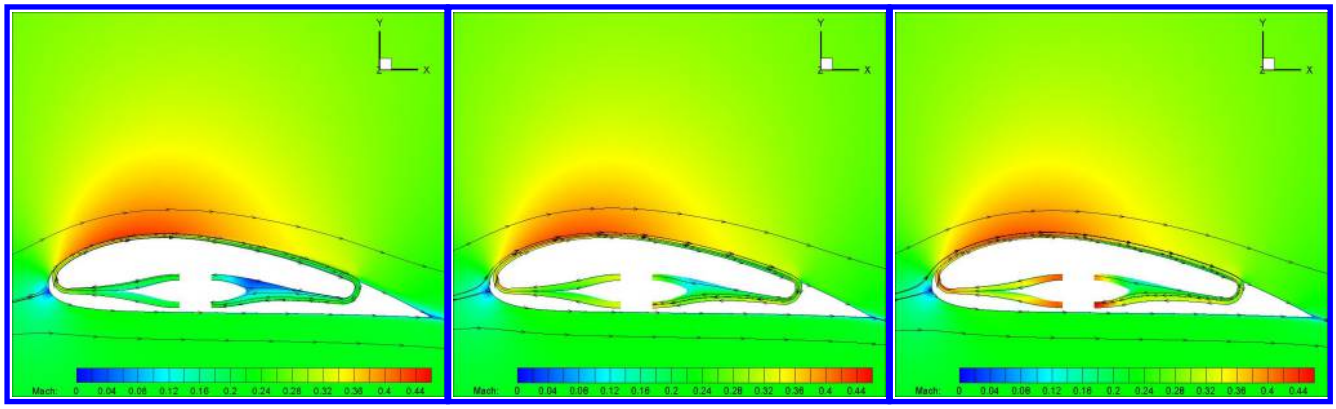

(a) (b) (c)

Figure 8: Mach contours at the 50% spanwise location of ducts and airfoil for design (a)$W/D = 2.76$, (b)$W/D = 4.0$, and (c)$W/D = 5.0$

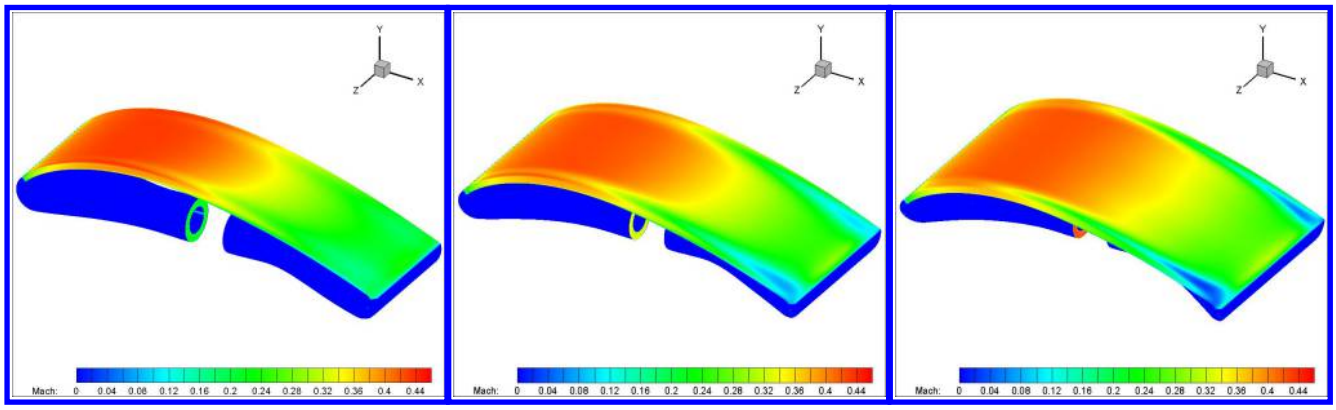

(a) (b) (c)

Figure 9: Mach contours of ducts and airfoil suction surface for design (a)$W/D = 2.76$, (b)$W/D = 4.0$, and (c)$W/D = 5.0$

The isentropic Mach number (M_{isen}) distributions are plotted at various spanwise locations of the airfoil surface in figure 10. The curve discontinuities demonstrate the locations of the injection and suction slots. At the 5% span, M_{isen} is lower for the higher width-diameter ratios, and is also lower than at the other spans. This is because the jet momentum of the high W/D ducts is weaker near the CFJ duct sides. After the suction slot, the isentropic Mach number stays almost constant towards the trailing edge for the two higher widths due to the mild flow separation occurring there. At 25% span, M_{isen} for $W/D = 4.0$ and 5.0 decrease toward the trailing edge but are still higher than for $W/D = 2.76$. At 50% span, the the isentropic Mach numbers have a more similar distribution

but still the one for $W/D = 2.76$ is still slightly higher due to the overall slightly stronger jet momentum due to less loss on the two sides.

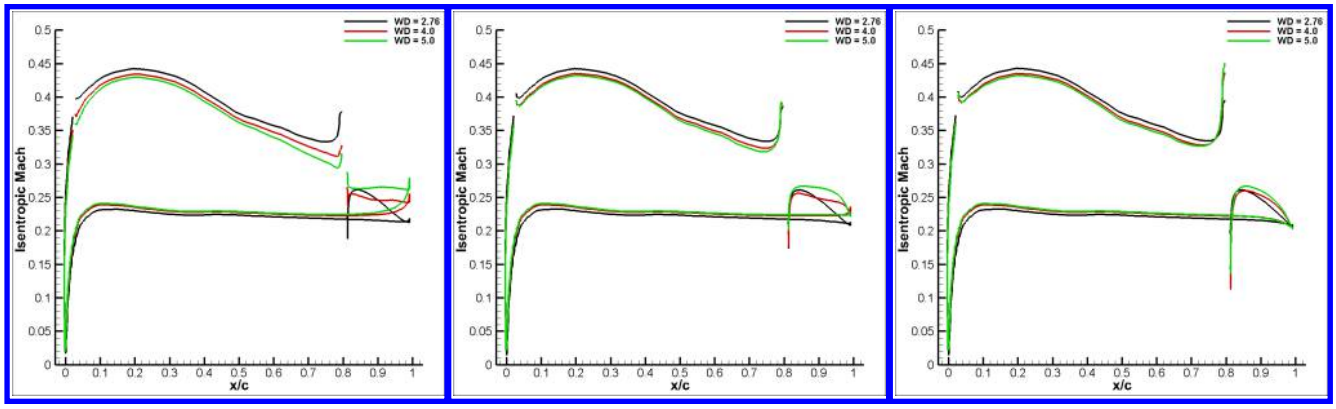

(a) (b) (c)

Figure 10: Isentropic Mach distributions on the airfoil surface at (a)5%, (b)25%, and (c)50% span

The total pressure recoveries for each duct is shown in figure 11. The smaller $W/D = 2.76$ design shows excellent recovery of 99% for injection and 99.1% for suction. $W/D = 4.0$ shows a 0.7 point decrease in injection and suction recoveries, 98.3% and 98.4% respectively. The total pressure recovery for $W/D = 5.0$ continues to decrease, with 97.6% for the injection duct and 97.9% for the suction duct. While the differences may seem slight, when it comes to a CFJ system it makes a significant difference since the micro-compressor total pressure is typically very small at cruise condition (e.g., 1.04). A small total pressure loss in the duct will substantially decrease the overall system efficiency.

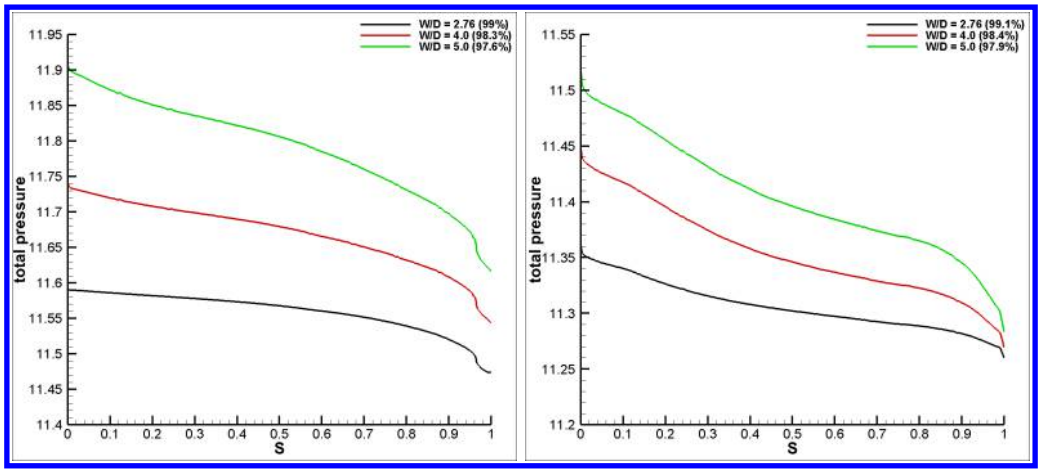

(a) (b)

Figure 11: Total pressure distributions for (a)injection and (b)suction ducts

Figures 12 and 13 show the Mach number contours of the 2D flow slices in the streamwise and transverse directions respectively for the injection and suction ducts. For $W/D = 5.0$, the mass flow rate is much larger than $W/D = 2.76$. Since the compressor outlet has the same area, the Mach number of $W/D = 5.0$ is substantially higher than that of $W/D = 2.76$ as shown in both figures 12 and 13. The high Mach number creates more total pressure loss as shown in figure 11. Benefited from the more converging area, the suction duct with $W/D = 5.0$ actually has better attached flow than that of $W/D = 2.76$ as shown in figures 8, 12, and 13. Figure 14 shows

the Mach contours on the vertical mid-cross-section, which shows that the Mach number is high at the entrance of the injection duct. The high momentum flow is not spread enough to the side walls at the injection slot. Figure 15 shows the Mach number contours near the lower suction duct wall, which indicates the low momentum flow (in blue) for $W/D = 4.0$ and 5.0 propagating from the airfoil outside of the duct demonstrated in figure 9. The weakened flows in the corner of the suction slot for $W/D = 4.0$ and 5.0 appear to be caused by the weak injection momentum near the two side walls shown in figure 14. For all three designs, the injection ducts have attached flows. The suction duct figures show a weak and low momentum region above the bullet centerbody for $W/D = 2.76$, but the flow is not separated (figures 12 and 13).

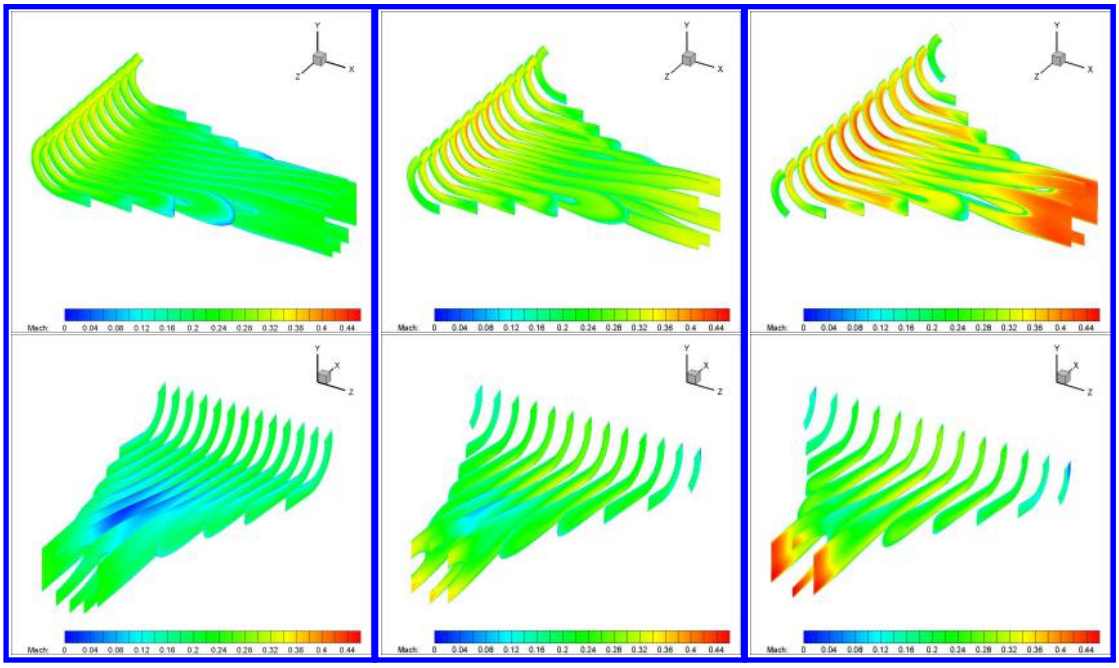

(a) (b) (c)

Figure 12: 2D Mach contour flow slices in the Z-direction for injection (top) and suction (bottom) ducts for design (a)$W/D = 2.76$, (b)$W/D = 4.0$, and (c)$W/D = 5.0$

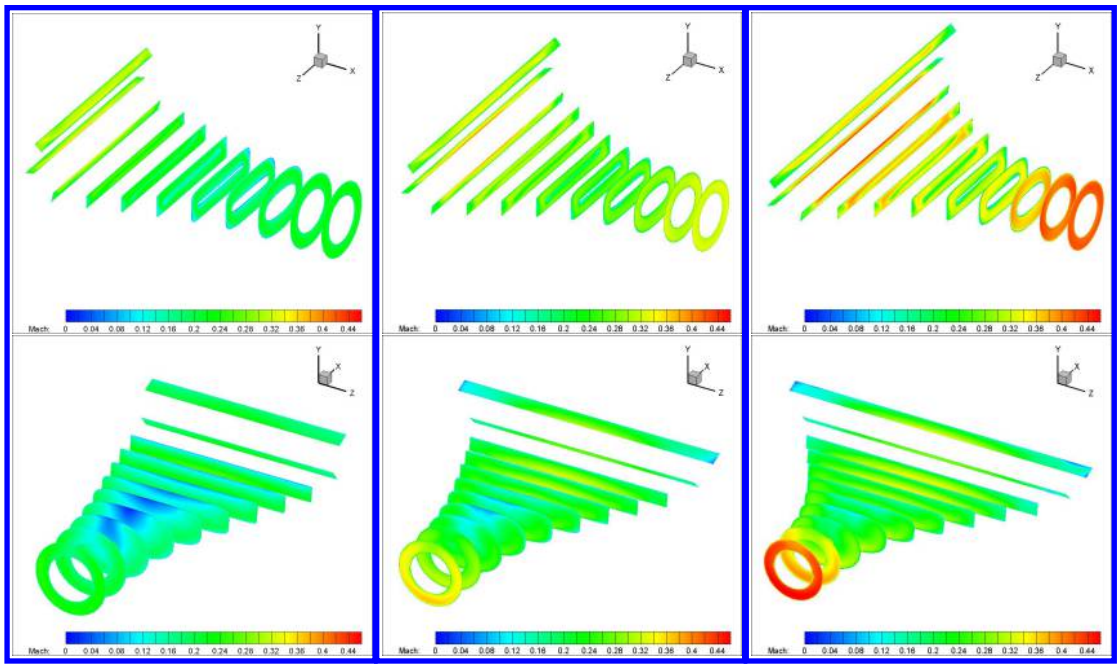

(a) (b) (c)

Figure 13: 2D Mach contour flow slices in the transverse direction for injection (top) and suction (bottom) ducts for design (a)$W/D = 2.76$, (b)$W/D = 4.0$, and (c)$W/D = 5.0$

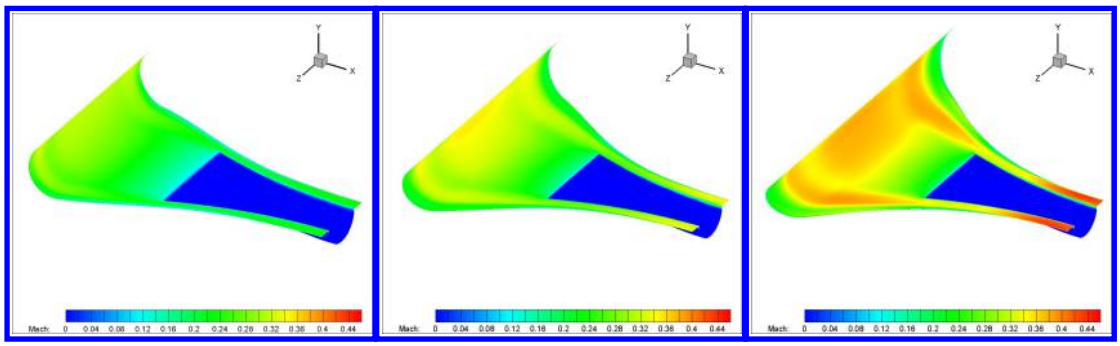

(a) (b) (c)

Figure 14: 2D Mach contour flow along the mean line for the injection duct for design (a)$W/D = 2.76$, (b)$W/D = 4.0$, and (c)$W/D = 5.0$

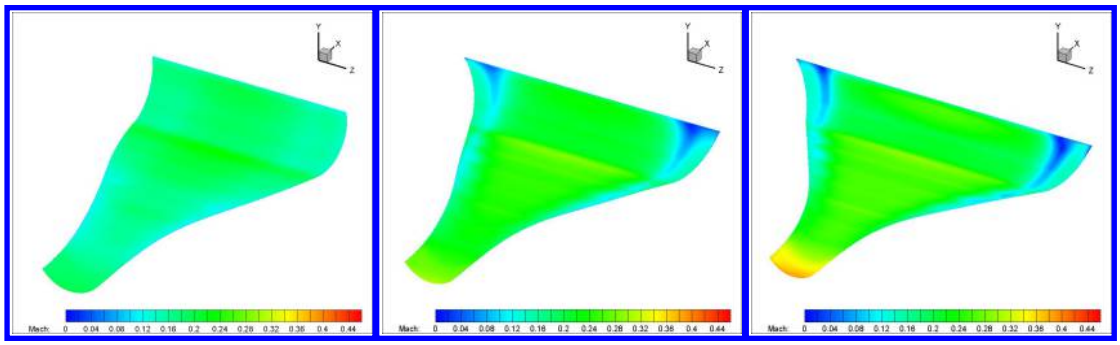

(a) (b) (c)

Figure 15: 2D Mach contour flow along the bottom surface of the suction duct for design (a)$W/D = 2.76$, (b)$W/D = 4.0$, and (c)$W/D = 5.0$

To determine the cause of the corner flow separation at higher widths, a study was done with a completely rectangular injection duct and a suction duct transitioning from rectangular to circular surfaces at $W/D = 4.0$ (labeled as $W/D = 4.0$ $RDinj$), $M = 0.25$, $AoA = 5°$, and $C_\mu = 0.03$. The rectangular injection duct has a constant width from inlet to outlet, and a uniform flow entering through the inlet. Figure 16 shows the mesh used as well as flow fields at the 50% spanwise location and the airfoil suction surface. The corner separation is completely removed and the flow is very uniform and symmetrical throughout the span. This points to the injection duct being the cause of the separation in the previous cases. The flow needs to exit the injection duct more uniformly in order to maintain a healthy flow downstream of the airfoil before it reaches the suction duct.

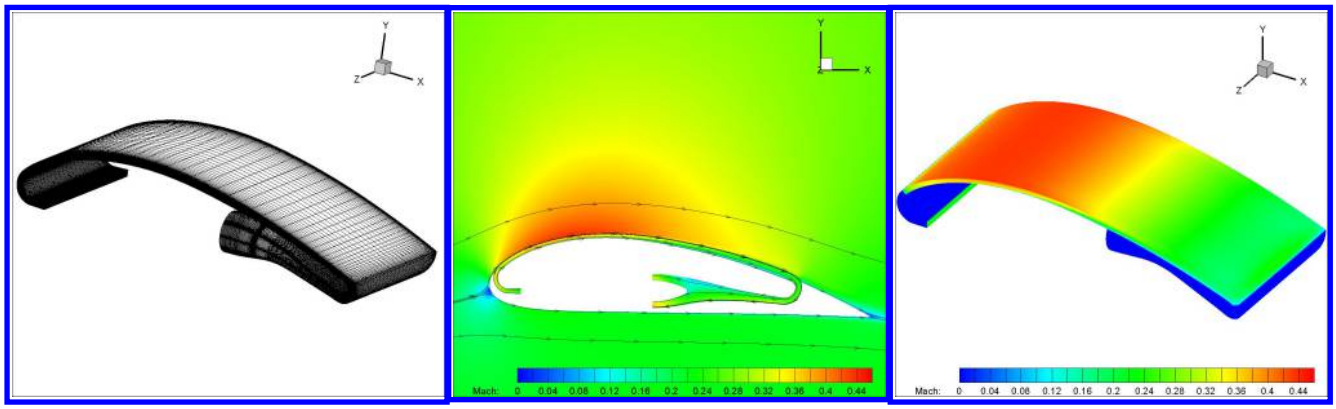

(a) (b) (c)

Figure 16: (a) Mesh of 3D CFJ airfoil with a rectangular injection duct, (b) Mach contour at the 50% spanwise location, (c) Mach contour of ducts and airfoil suction surface for $W/D = 4.0$ $RDinj$

To further study why the corner separation occurs, the streamwise velocity at the injection duct outlet was plotted in figure 17 for all the cases studied thus far. The span is normalized by the width. The plot shows the cases of $W/D = 2.76$ and $W/D = 4.0$ $RDinj$ exhibiting a "wolf-ear" phenomenon where the maximum velocity is reached at the sides of the duct, greater than at the middle of the span. Conversely, the cases of $W/D = 4.0$ and 5.0 that have the corner separation, show the velocity at the sides of the airfoil being lower than at the middle, and lower than $W/D = 2.76$ and $W/D = 4.0$ $RDinj$. This suggests that the corner separations are due to weakened velocity at the sides of the injection outlet that propagate into separated flow further downstream. The design of the injection duct is then supremely important. Examining figure 6, shows the final 20% of the injection a distribution for $W/D = 2.76$ becoming more horizontal and therefore more rectangular towards the outlet, similar

to $W/D = 4.0$ $RDinj$. However, the other two designs continue sharp slopes until the end. It is presumed then, that the key to removing the corner separation and still maintaining a high width-to-diameter ratio lies in having a constant width a distribution approaching the injection outlet in order to push the flow more towards the injection duct sides.

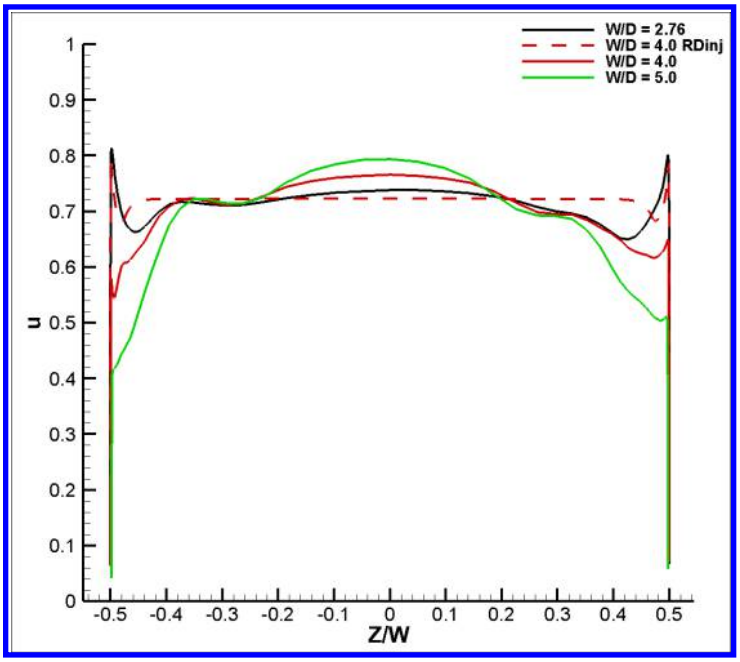

Figure 17: Streamwise velocities at the injection duct outlet

Angle of attack 5° was simulated at a C_μ of 0.03 as per [15, 32]. The performance results of the numerical simulation for all cases are shown in table 2 below, with a baseline airfoil with no CFJ at $W/D = 2.76$ included for comparison, (labeled as $W/D = 2.76$ BL). Using CFJ for $W/D = 2.76$ increases the lift coefficient by 27% and decreases the drag coefficient by 35% compared to the baseline. It is also evident that the performance between $W/D = 2.76$ and $W/D = 4.0$ $RDinj$ is very comparable. Only considering designs $W/D = 2.76, 4.0$, and 5.0, the highest CFJ corrected aerodynamic efficiency is 62.48 from design $W/D = 2.76$. The larger W/D designs do not have nearly as good a performance, with about 38% decrease for $W/D = 4.0$ and a 55% decrease for $W/D = 5.0$. The primary reason for the decreased C_L/C_{Dc} is that the power coefficient is substantially increased, 41% more for $W/D = 4.0$ and 85% more for $W/D = 5.0$, detailing how even though the difference in total pressure recoveries was about 1%, the slightest total pressure loss can result in dramatic increases to the CFJ power consumption as evidenced by Eq. (7).

Table 2: Performance of each duct design at $M = 0.25$

W/D	C_μ	C_L	C_D	P_C	C_L/C_D	C_L/C_{Dc}	C_L^2/C_{Dc}	P_{tr}
2.76 BL	N/A	1.028	0.019	N/A	52.78	52.78	54.24	N/A
2.76	0.03	1.303	0.013	0.008	103.47	62.48	81.41	1.028
4.0 RDinj	0.03	1.328	0.013	0.008	105.76	63.45	84.27	1.029
4.0	0.03	1.194	0.019	0.012	63.12	39.03	46.61	1.039
5.0	0.03	1.163	0.026	0.015	43.97	27.85	32.38	1.052

4 Conclusion

This paper conducts a design study for the CFJ injection and suction ducts utilized in the design process of an integrated system of 3D CFJ airfoil and micro-compressor to maximize the W/D with optimal aerodynamic efficiency. The injection duct inlet is simulated with a swirl profile provided from the micro-compressor design. The cruise condition simulation is at Mach number 0.25 and angle of attack 5°.

A duct design of $W/D = 2.76$ achieves well-attached flow field and total pressure recoveries of 99% for injection and 99.1% for suction duct. It also has a very high corrected aerodynamic efficiency. Increasing to $W/D = 4.0$ decreases the total pressure recoveries to 98.3% for injection and 98.4% for suction duct. It also has a weak flow emerging on the corner of the airfoil surface before the suction duct inlet, and the corrected aerodynamic efficiency was significantly less. At $W/D = 5.0$, the injection duct had a total pressure recovery of 97.6% and the suction duct was 97.9%, with an even lower corrected aerodynamic efficiency and greater corner separation. Both $W/D = 4.0$, and 5.0 had lower corrected aerodynamic efficiencies than the baseline airfoil.

Simulating a case of $W/D = 4.0$ with a rectangular injection duct shape leads to the conjecture that the cause of the corner separation is the injection duct design. It is desirable to have stronger injection jet velocity near the two injection side walls with a "wolf-ear" shape injection velocity profile. To achieve this, the injection duct needs to have a constant a width approaching the outlet. This is crucial for the design of high width-to-diameter ratio ducts for a 3D CFJ airfoil. More work to optimize the duct design is in progress.

5 Acknowledgement

The authors would like to acknowledge the computing resources provided by the Center of Computational Sciences (CCS) at the University of Miami. The teaching assistantship support from the University of Miami is also acknowledged.

Disclosure: The University of Miami and Dr. Gecheng Zha may receive royalties for future commercialization of the intellectual property used in this study. The University of Miami is also equity owner in CoFlow Jet, LLC, licensee of the intellectual property used in this study.

References

[1] G. Zha, and C.D. Paxton, "A Novel Flow Control Method for Airfoil Performance Enhancement Using Co-Flow Jet," *Applications of Circulation Control Technologies, AIAA Book Series, Progress in Aeronautics and Astronautics*, vol. Vol. 214, Chapter 10, pp. 293–314, 2006.

[2] G. Zha, W. Gao, and C.D. Paxton, "Jet Effects on Co-Flow Jet Airfoil Performance," *AIAA Journal*, vol. 45, pp. 1222–1231, 2007.

[3] G.-C. Zha, C. Paxton, A. Conley, A. Wells, and B. Carroll, "Effect of Injection Slot Size on High Performance Co-Flow Jet Airfoil," *AIAA Journal of Aircraft*, vol. 43, pp. 987–995, 2006.

[4] G.-C. Zha, B. Carroll, C. Paxton, A. Conley, and A. Wells, "High Performance Airfoil with Co-Flow Jet Flow Control," *AIAA Journal*, vol. 45, pp. 2087–2090, 2007.

[5] Wang, B.-Y. and Haddoukessouni, B. and Levy, J. and Zha, G.-C., "Numerical Investigations of Injection Slot Size Effect on the Performance of Co-Flow Jet Airfoil," *Journal of Aircraft*, vol. Vol. 45, No. 6,, pp. pp.2084–2091, 2008.

[6] B. P. E. Dano, D. Kirk, and G.-C. Zha, "Experimental Investigation of Jet Mixing Mechanism of Co- Flow Jet Airfoil." AIAA-2010-4421, 5th AIAA Flow Control Conference, Chicago, IL, 28 Jun - 1 Jul 2010.

[7] B. P. E. Dano, G.-C. Zha, and M. Castillo, "Experimental Study of Co-Flow Jet Airfoil Performance Enhancement Using Micro Discreet Jets." AIAA Paper 2011-0941, 49th AIAA Aerospace Sciences Meeting, Orlando, FL, 4-7 January 2011.

[8] A. Lefebvre, B. Dano, W. Bartow, M. Fronzo, and G. Zha, "Performance and energy expenditure of coflow jet airfoil with variation of mach number," *Journal of Aircraft*, vol. 53, no. 6, pp. 1757–1767, 2016.

[9] A. Lefebvre and G. Zha, "Numerical simulation of pitching airfoil performance enhancement using co-flow jet flow control," *AIAA 31st Applied Aerodynamics Conference*, vol. 2517, 2013.

[10] A. Lefebvre and G. Zha, "Co-flow jet airfoil trade study part i : Energy consumption and aerodynamic performance," *AIAA 32nd Applied Aerodynamics Conference*, vol. 2682, 2014.

[11] A. Lefebvre and G. Zha, "Co-flow jet airfoil trade study part ii : Moment and drag," *AIAA 32nd Applied Aerodynamics Conference*, vol. 2683, 2014.

[12] Y. Ren and G.-C. Zha, "Simulation of 3D Co-Flow Jet Airfoil with Embedded Micro-Compressor Actuator." AIAA Paper 2018-0330, 2018 AIAA Aerospace Sciences Meeting, AIAA SciTech Forum, Kissimmee, Florida, 8-12 January 2018.

[13] Y. Wang and G.-C. Zha, "Study of 3D Co-flow Jet Wing Induced Drag and Power Consumption at Cruise Conditions." AIAA Paper 2019-0034, AIAA SciTech 2019, San Diego, CA, January 7-11, 2019.

[14] Y. Wang, Y.-C. Yang, and G.-C. Zha, "Study of Super-Lift Coefficient of Co-Flow Jet Airfoil and Its Power Consumption." AIAA Paper 2019-3652, AIAA Aviation 2019, AIAA Applied Aerodynamics Conference, Dallas, Texas, 17-21 June 2019.

[15] Y. Wang and G.-C. Zha, "Study of Mach Number Effect for 2D Co-Flow Jet Airfoil at Cruise Conditions." AIAA Paper 2019-3169, AIAA Aviation 2019, AIAA Applied Aerodynamics Conference, Dallas, Texas, 17-21 June 2019.

[16] Yang, Yunchao and Zha, Gecheng, "Super-Lift Coefficient of Active Flow Control Airfoil: What is the Limit?," *AIAA Paper 2017-1693, AIAA SCITECH2017, 55th AIAA Aerospace Science Meeting, Grapevine, Texas*, p. 1693, 9-13 January 2017.

[17] J. R. Burley II, L. S. Bangert, and J. R. Carlson, "Static investigation of circular-to-rectangular transition ducts for high-aspect-ratio nonaxisymmetric nozzles." NASA Technical Paper 2534, 1986.

[18] Y. Ren and G.-C. Zha, "Design of Injection and Suction Ducts for Co-Flow Jet Airfoils with Embedded Micro-Compressors Actuator." AIAA Aviation Forum, 2018 Flow Control Conference, Atlanta, Georgia, 25-29 June 2018.

[19] Y. Ren and G.-C. Zha, "Design of Injection Jet Span Profile for Co-Flow Jet Airfoil." AIAA SciTech 2019 Forum, San Diego, California, 7-11 January 2019.

[20] P. R. Spalart and S. R. Allmaras, "A one-equation turbulence model for aerodynamic flows," in *30th Aerospace Sciences Meeting and Exhibit, Aerospace Sciences Meetings, Reno, NV, USA, AIAA Paper 92-0439*, 1992.

[21] Shen, Y.Q., and Zha, G.C., "Large Eddy Simulation Using a New Set of Sixth Order Schemes for Compressible Viscous Terms," *Journal of Computational Physics*, vol. 229, pp. 8296–8312, doi:10.1016/j.jcp.2010.07.017, 2010.

[22] Zha, G.C., Shen, Y.Q. and Wang, B.Y., "An improved low diffusion E-CUSP upwind scheme ," *Journal of Computer and Fluids*, vol. 48, pp. 214–220, Sep. 2011.

[23] Y.-Q. Shen and G.-Z. Zha , "Generalized finite compact difference scheme for shock/complex flowfield interaction," *Journal of Computational Physics*, vol. doi:10.1016/j.jcp.2011.01.039, 2011.

[24] Shen, Y.Q., Zha, G.C., and Wang, B.Y., "Improvement of Stability and Accuracy of Implicit WENO Scheme," *AIAA Journal*, vol. 47, pp. 331–334, DOI:10.2514/1.37697, 2009.

[25] Shen, Y.Q., Zha, G.C., and Chen, X., "High Order Conservative Differencing for Viscous Terms and the Application to Vortex-Induced Vibration Flows," *Journal of Computational Physics*, vol. 228(2), pp. 8283–8300, doi:10.1016/j.jcp.2009.08.004, 2009.

[26] Shen, Y.Q., and Zha, G.C., "Improvement of the WENO Scheme Smoothness Estimator," *International Journal for Numerical Methods in Fluids*, vol. 64,, pp. 653–675, DOI:10.1002/fld.2186, 2009.

[27] Zha, G.C., and Bilgen, E., "Numerical Study of Three-Dimensional Transonic Flows Using Unfactored Upwind Relaxation Sweeping Algorithm," *Journal of Computational Physics*, vol. 125, pp. 425–433,, 1996.

[28] Wang, B.Y., Hu, Z. and Zha, G.C., "A General Sub-Domain Boundary Mapping Procedure For Structured Grid CFD Parallel Computation," *AIAA Journal of Aerospace Computing, Information, and Communication*, vol. 5, pp. 425–447, 2008.

[29] Y.-Q. Shen, G.-C. Zha, and B.-Y. Wang, "Improvement of Stability and Accuracy of Implicit WENO Scheme," *AIAA Journal*, vol. 47, pp. 331–344, 2009.

[30] P. Barrios, Y. Ren, K. Xu, and G.-C. Zha, "Design of 3D Co-Flow Jet Airfoil with Integrated Micro-Compressor for High Operating Efficiency at Cruise Condition." AIAA Paper 2021-2581, AIAA Aviation 2021, AIAA Aviation 2021 Forum, Virtual Event, 2-6 August 2021.

[31] P. Barrios, Y. Ren, K. Xu, and G.-C. Zha, "Integration of Co-Flow Jet Airfoil with Quasi-Micro-Compressor for High Efficiency Cruise at Different Mach Numbers." AIAA Paper 2022-1299, AIAA SciTech 2022, AIAA SciTech 2022 Forum, San Diego, California, 3-7 January 2022.

[32] Y. Wang and G.-C. Zha, "Study of Mach Number Effect for 3D Co-Flow Jet Wings at Cruise Conditions." AIAA Paper 2020-0045, AIAA SciTech 2020, AIAA SciTech 2020 Forum, Orlando, Florida, 6-10 January 2020.